

Cite this: *J. Mater. Chem. A*, 2022, 10, 1861

Structural dynamics of Schottky and Frenkel defects in ThO₂: a density-functional theory study†

Samuel Moxon,¹ Jonathan Skelton,¹ Joshua S. Tse,¹ Joseph Flitcroft,¹ A. Togo,² David J. Cooke,³ E. Lora da Silva,⁴ Robert M. Harker,⁵ Mark T. Storr,⁶ Stephen C. Parker⁷ and Marco Molinari^{1*}

Thorium dioxide (ThO₂) is a promising alternative to mixed-oxide nuclear fuels due to its longer fuel cycle and resistance to proliferation. Understanding the thermal properties, in particular the thermal conductivity, under reactor conditions is critical to the success of any candidate fuel material. ThO₂ has a higher thermal conductivity and thus a lower operating temperature than other fuel systems. However, the presence of defects in real materials directly influences the structural dynamics and physical properties, and the impact of defects on the properties of ThO₂ is largely unexplored. We have employed density-functional theory calculations to study the structure and energetics of the intrinsic Schottky and Frenkel defects in ThO₂ and their impact on the thermophysical properties. We identify the anion Frenkel defect to be the most stable, and we identify characteristic spectral signatures of the defects in the phonon dispersions and infrared spectra. We further employ two approximate models to assess the impact of the defects on the thermal transport and find that both types of defect are predicted significantly to reduce the thermal conductivity. The methodology we present facilitates the prediction of the thermophysical and transport properties of defective materials at an atomistic level, and should be readily transferrable to existing and in-development nuclear fuel systems.

Received 24th November 2021
Accepted 5th January 2022

DOI: 10.1039/d1ta10072f

rsc.li/materials-a

1. Introduction

As fossil fuels are phased out in favour of renewable energy to limit global warming,¹ nuclear power plays an increasingly critical role in meeting worldwide energy demand. Thorium-based fuels are ideal candidates to address this challenge, due to the potential safety and economic benefits compared to more traditional actinide-dioxide fuels such as UO₂. ThO₂ can be used in mixed-

oxide (MOX) fuels with uranium or plutonium to improve reactor safety, as its higher thermal conductivity results in a lower operating temperature and prevents overheating.^{2,3} ThO₂ also reduces the risk of proliferation and the amount of highly radioactive spent fuel waste generated. Indeed, due to its large domestic supply of thorium (up to a third of global reserves),³ India has positioned itself to take full advantage of these benefits by aiming to use ThO₂ in advanced heavy water reactors (AHWRs).⁴

A complete understanding of the thermophysical properties of ThO₂ is critical to controlling fuel performance at the high temperatures and pressures in nuclear reactors. An important consideration here is the defect chemistry. The energy release associated with nuclear events in reactors can generate large non-equilibrium concentrations of defects, and these can have a direct influence on the physical properties. Since experimental measurements on ThO₂ are challenging, computational modelling using first-principles methods such as density-functional theory (DFT), in conjunction with modern high-performance computing (HPC), plays a key role in contemporary nuclear research, particularly when atomistic or nanoscale details are required.⁵

Under ambient conditions ThO₂ is non-magnetic with a cubic structure in the *Fm* $\bar{3}$ *m* space group (no. 225).^{6–10} A phase transition to an orthorhombic *Pnma* structure (no. 62) begins at 20–30 GPa^{6–9} and completes at above 1000 K and 30 GPa.¹¹ As Mott insulators, the thermal transport in ThO₂ and other

¹Department of Chemical Sciences, University of Huddersfield, Queensgate, Huddersfield, HD1 3DH, UK. E-mail: m.molinari@hud.ac.uk

²Department of Chemistry, University of Manchester, Manchester M13 9PL, UK. E-mail: jonathan.skelton@manchester.ac.uk

³IFIMUP, Department of Physics and Astronomy, Faculty of Science, University of Porto, 4169-007, Porto, Portugal

⁴National Institute for Materials Science (NIMS), 1-2-1 Sengen, Tsukuba, Ibaraki 305-0047, Japan

⁵AWE Aldermaston, Reading, RG7 4PR, UK

⁶Department of Chemistry, University of Bath, Claverton Down, Bath, BA2 7AY, UK

† Electronic supplementary information (ESI) available: Comparison of the ΔA_T computed using methods 1 and 2; simulated Raman spectrum of stoichiometric ThO₂; convergence of the harmonic CRTA functions of the pristine and defective supercells as a function of the *q*-point sampling mesh; comparison of CRTA calculations on the primitive cell and supercell of stoichiometric ThO₂ with our selected *q*-point sampling; convergence of the wJDOS functions with respect to *q*-point sampling; comparison of the PDOS curves of stoichiometric ThO₂ and the defective models; and effect of grain size on the thermal conductivity of the defect models for comparison to pristine ThO₂. See DOI: 10.1039/d1ta10072f



actinide oxides is controlled by heat transport through phonons.^{12,13} The thermal conductivity is however generally low for oxide materials due to the limited transport through the F_{2g} mode, despite its large mode group velocity.¹² There is also relatively little known about how defects might impact the thermal transport, although a recent study of Deskins *et al.*¹⁴ predicts a decrease in the thermal conductivity of ThO_2 from point defects including oxygen and thorium vacancies. This has also been observed in other work on ThO_2 (ref. 15 and 16) and UO_2 .^{17–19} While a variety of point defects and defect clusters can be found in fluorite structures, Schottky and Frenkel defects are simple, charge-neutral defects. These will both be produced under reactor operating conditions, and are likely to have an impact on the thermal conductivity,^{15,19} but unravelling this at the nanoscale requires computational approaches since disentangling the effects of specific defects using experimental approaches is challenging and currently limited.

In this work, we use DFT modelling to perform a comprehensive study of the intrinsic defects in ThO_2 and to assess their impact on the structural dynamics. Whereas the structural dynamics of stoichiometric ThO_2 are well documented,^{20–24} little is currently known of defective ThO_2 due to the computational challenges inherent in studying defective systems. We model the phonon dispersion and density of states of stoichiometric ThO_2 and compare these to models with intrinsic Schottky and Frenkel defects. This allows us to determine key spectral signatures for identifying these defects in material samples. We also quantify the impact of the lattice dynamics on the defect

formation thermodynamics. Finally, we estimate the potential impact of the defects on thermal transport, which is an important material property both for reactor design and the storage of waste material.

II. Methods

DFT calculations were performed using the Vienna *Ab initio* Simulation Package (VASP) code.²⁵

A 96-atom $2 \times 2 \times 2$ supercell expansion of the 12-atom ThO_2 conventional unit cell was constructed and used to build models of three intrinsic defects, namely cation (Th) Frenkel, anion (O) Frenkel and Schottky defects, with different relationships between the vacancy/interstitial sites (Fig. 1). For comparison with the literature and to verify that our choice of cell size was appropriate we also modelled the defects in $3 \times 3 \times 3$ supercells with 324 atoms.

The spin-polarised simulations used a plane-wave basis set with the electron-ion interactions described using projector augmented-wave (PAW) pseudopotentials^{26,27} with frozen [Xe] and [He] cores for Th and O respectively. The plane-wave cutoff was set to 500 eV. Exchange–correlation effects were treated using the revised Perdew–Burke–Ernzerhof generalised gradient approximation functional for solids (PBEsol),²⁸ without the use of a Hubbard U correction, following previous studies on ThO_2 .^{22,29–31} Spin–orbit coupling was not included as this has been shown to have a comparatively small effect in ThO_2 .³² The Brillouin zone of the 12-atom ThO_2 conventional cell was

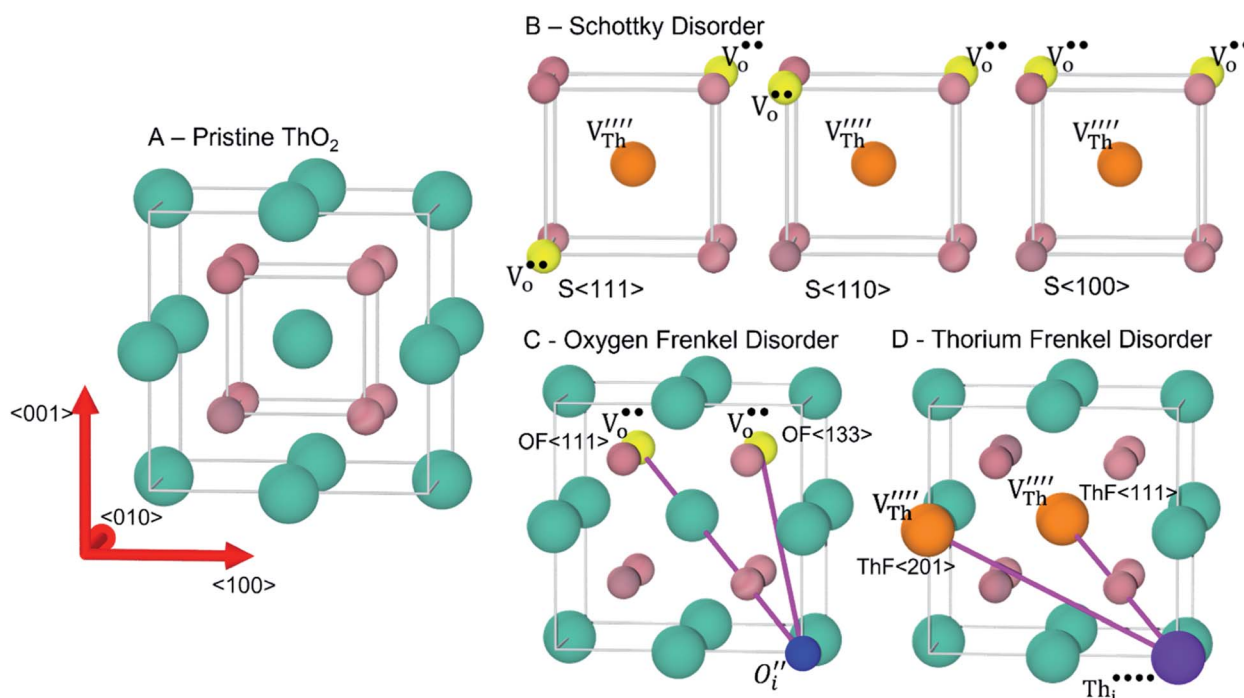


Fig. 1 Intrinsic ThO_2 defects investigated in this work: (A) pristine ThO_2 with the Th and O atoms in green and pale pink respectively; (B) three Schottky defect models ($V_{\text{Th}}''' + 2V_{\text{O}}''''$) with the V_{Th}''' and V_{O}'''' shown in orange and yellow and arranged along the $\langle 111 \rangle$, $\langle 110 \rangle$ and $\langle 100 \rangle$ directions;^{42–45} (C) two O Frenkel defect models with the O_i'' and V_{O}'''' (blue/yellow) arranged along the $\langle 111 \rangle$ and $\langle 133 \rangle$ directions; and (D) two Th Frenkel defect models with the Th_i'''' and V_{Th}''' (purple/orange) arranged along the $\langle 111 \rangle$ and $\langle 201 \rangle$ directions.



sampled using a Γ -centred Monkhorst–Pack k -point grid³³ with $4 \times 4 \times 4$ subdivisions, which was proportionally reduced to a $2 \times 2 \times 2$ sampling for the $2 \times 2 \times 2$ and $3 \times 3 \times 3$ supercells.

Pristine ThO_2 was geometry optimised at constant pressure to tolerances of 10^{-8} eV and 10^{-3} eV \AA^{-1} on the electronic energy and ionic forces respectively. The defective models were optimised with the cell shape and volume fixed to that of the equivalent supercell of the geometry optimized pristine ThO_2 .

To model the lattice dynamics, the 2nd-order harmonic interatomic force constants (IFCs) were obtained using the finite-displacement approach implemented in the Phonopy code³⁴ with VASP as the force calculator. The displacements were generated in the 96-atom cells used for the stoichiometric and defective models. The atom-projected phonon density of states (PDOS) curves for the models were evaluated on Γ -centred grids of $10 \times 10 \times 10$ phonon wavevectors (q -points). For the stoichiometric model, a transformation matrix was used to convert to the three-atom primitive cell to evaluate the phonon dispersion. For the defective models, we made use of the band unfolding methodology^{35,36} implemented in the Phonopy code to project the dispersions onto the ThO_2 primitive cell for comparison to the stoichiometric structure. A non-analytical correction was applied using Born effective charges and high-frequency dielectric constants computed with the density-functional perturbation theory (DFPT) routines in VASP.³⁷ To evaluate the IR and Raman activities of the Γ -point phonon modes, we used the Phonopy-spectroscopy project,³⁸ which is documented in ref. 39. Brief details of the methodology used for simulating the IR and Raman spectra are given in the ESI.†

The Phono3py code⁴⁰ was used to compute the thermal conductivity of stoichiometric ThO_2 within the single-mode relaxation-time approximation by calculating the 3rd-order IFCs using the 96-atom supercell. The phonon group velocities, lifetimes and thermal conductivity were deemed to be converged with a $48 \times 48 \times 48$ sampling mesh for the ThO_2 primitive cell. As described in the text, we then estimated the thermal conductivity of the 96-atom defect models using one of two approximate models.⁴¹ In principle, a q -point mesh with $15 \times 15 \times 15$ subdivisions should be adequate for sampling the $32 \times$ smaller Brillouin of the supercells. However, we were only able to use a smaller mesh with $10 \times 10 \times 10$ subdivisions due to memory constraints. As discussed in the text below, we estimate that this leads to an error in the calculated properties on the order of 20%. Finally, we also generated for the supercell models two-phonon weighted joint density of states (w-JDOS) functions, using the same $10 \times 10 \times 10$ mesh.

We note that our chosen supercell size may have an impact on the structural dynamics calculations, *i.e.* the calculated frequencies, simulated phonon spectra, and predicted thermal transport. However, the substantial workload means that it is computability infeasible to perform these calculations on the larger $3 \times 3 \times 3$ defect supercell models, so we are unable to quantify the impact as we do for the defect-formation energies.

III. Results and discussion

A. Structures of the stoichiometric and defective systems

Our calculated lattice constant for stoichiometric ThO_2 (Fig. 1A) is 5.5605 \AA , compared to the experimental range of 5.5921–5.604 \AA .^{6,46–50} Standard (athermal) DFT does not take into account the effect of temperature. An experimental lattice parameter of 5.5828 \AA at 0 K can be extrapolated from the empirical function of Tyagi and Mathews,⁵¹ which is still higher than our calculated value. This indicates that the underestimation of the lattice parameter may be due to the DFT functional used.

The Schottky defect involves the removal of a complete ThO_2 formula unit to create two oxygen vacancies and a Th vacancy ($V_{\text{Th}}''' + 2V_{\text{O}}''$) according to:



Following Govers *et al.*⁴⁵ we considered only the first nearest-neighbour positions for the vacancies. We investigated three potential arrangements where the two V_{O}'' are arranged along the $\langle 111 \rangle$, $\langle 110 \rangle$ and $\langle 100 \rangle$ directions with respect to the central V_{Th}''' , which we denote S $\langle 111 \rangle$, S $\langle 110 \rangle$ and S $\langle 100 \rangle$ respectively (Fig. 1B).

The cation and anion Frenkel defects are a type of intrinsic disorder and involve the formation of pairs of vacancies and interstitials according to:



To prevent spontaneous recombination during the geometry optimisation, the interstitial and vacancy must not be adjacent. As shown in Fig. 1C, we therefore created O Frenkel defects with the O_i' and V_{O}'' arranged as 2nd-nearest neighbours along the $\langle 111 \rangle$ and $\langle 133 \rangle$ directions. These configurations, which we refer to as OF $\langle 111 \rangle$ and OF $\langle 133 \rangle$, are equivalent to those examined in other literature.^{42,43,45} In our Th Frenkel models (Fig. 1D), the Th_i'''' and V_{Th}''' are arranged along the $\langle 111 \rangle$ and $\langle 201 \rangle$ directions, which we denote ThF $\langle 111 \rangle$ and ThF $\langle 201 \rangle$ respectively. The ThF $\langle 201 \rangle$ has previously been studied,^{42,43,45} but as discussed below our calculations predict the ThF $\langle 111 \rangle$ configuration to be energetically more stable.

B. Defect formation energies

The calculated defect formation energies are presented and compared to other computational studies in Table 1.

Experimental studies of the O Frenkel disorder indicate defect formation enthalpies in the range of 2.28–4.68 eV from diffusion measurements using the isotope-exchange method,⁵² and a value of 4.2 eV from fitting high-temperature heat capacity data.⁵³ These are a good match to our calculated formation energy of 4.42 eV for the most stable OF $\langle 133 \rangle$ defect. The higher stability of the OF $\langle 133 \rangle$ defect compared to the OF $\langle 111 \rangle$ also agrees with potential-model (PM) calculations using larger $4 \times$



Table 1 Formation energies (eV) for the Schottky and Th/O Frenkel defects examined in this study compared to other theoretical literature. The ThF_∞ and OF_∞ structures denote defect energies corrected to the infinite dilution limit. The size of the supercell used in the calculations is given in the first row of the table. Comparison studies are identified as being performed using DFT, as in the present work, or using classical potential models (PM). Where available, athermal energies are also compared to free energies computed at T = 1000 K

Supercell	2 × 2 × 2		3 × 3 × 3			4 × 4 × 4			5 × 5 × 5			
	This study (PBEsol, 1000 K)	This study (PBE, 1000 K)	DFT ⁴³ (PBE)	DFT ⁵⁹ (GGA + U)	PM ⁴⁴	This study (PBEsol)	DFT ⁴³ (PBE, 1000 K)	PM ⁴⁴	PM ⁵⁵	PM ⁵⁶	PM ⁴⁴	PM ⁴⁴
S _∞	—	—	—	20.6	—	—	8.05	—	10.39	13.79	12.16–20.66	12.89
S(100)	5.49	5.73	5.08	—	7.65	5.93	5.04	7.53	—	7.39	7.07–12.49	7.51
S(110)	4.90	5.16	4.47	—	6.49	5.43	4.51	6.60	5.40	6.35	6.24–11.14	6.62
S(111)	5.01	5.29	4.66	—	6.45	5.37	4.51	6.41	5.41	6.05	6.09–10.85	6.39
ThF _∞	—	—	—	—	—	—	13.72	—	19.39	20.56	21.78–25.35	18.23
ThF(111)	12.53	12.57	—	—	—	—	—	—	—	—	—	—
ThF(201)	—	12.90	—	—	—	—	—	—	—	15.56	16.47–21.23	13.65
OF _∞	—	—	—	9.8	—	—	4.98	—	6.60	7.64	6.47–7.93	5.89
OF(111)	—	5.13	—	—	—	—	—	—	—	6.83	5.37–6.58	5.38
OF(133)	4.03	4.42	—	—	—	—	—	—	—	6.32	5.23–6.24	5.03

4 × 4⁴² and 5 × 5 × 5 supercells.⁴⁴ Ando *et al.* concluded that O Frenkel and Schottky defects would need to have energies of 2.82 eV and 4.2 eV, respectively in order to explain the self-diffusion behaviour measured in a ThO₂ single crystal, which indicates that the O transport is primarily *via* Frenkel defects.⁵⁴ This is the only experimental value we could find for the Schottky defect, but it is reassuring that it has been calculated to be higher in energy than the O Frenkel defect, thus supporting our DFT values (Table 1).

The Schottky defect has been studied computationally using DFT⁴³ and PMs using the shell,⁵⁵ rigid ion^{42,56,57} and embedded atom⁴⁴ formalisms. Using a 2 × 2 × 2 supercell, we predict defect formation energies between 5.16–5.73 eV, in the order S(110) < S(111) < S(100), in agreement with free-energy calculations on ThO₂ at 1000 K and 0.2 atm⁴³ and similar calculations on UO₂.⁵⁸ Although the energy differences between the configurations are marginal, the relative stabilities are changed when using larger supercells such that our 3 × 3 × 3 supercell models predict a stability order of S(111) < S(110) < S(100). PM calculations using larger supercells predict the same stability trends and small energy differences as our DFT calculations on larger cells. We attribute the differences between cell sizes to better screening of the coulombic repulsion between positively charged oxygen vacancies in the larger models.

For the Th Frenkel disorder, we find that the ThF(111) configuration is more stable than the ThF(201) defect examined in other literature,⁴⁵ although the formation energy of 12.57 eV makes this defect considerably less favourable than the Schottky and O Frenkel defects.

The trend in stability of the different Frenkel pair configurations appears to be related to the distance between the vacancy and interstitial: the more stable ThF(111) and OF(133) configurations have interstitial-vacancy distances of 4.48 and 5.87 Å, respectively, whereas the less stable ThF(201) and OF(111) configurations have larger separations of 5.96 and 6.88 Å. We therefore conclude that the closer the interstitial and vacancy sites are, the more stable the defect pair is, likely because shorter distances optimise the attractive coulombic interactions between the oppositely-charged point defects.

It is also of note that small supercells imply relatively high defect concentrations, and interactions between defects in neighbouring cells can lead to higher stabilities than when the formation energies are corrected to the infinite-dilution limit.^{22,42–44,55,56,59} The potential model studies in ref. 42 and 44 predict a qualitative stability ordering of OF < S < ThF, in agreement with our results. While the trend is unchanged when the formation energies are corrected to the infinite-dilution limit, the correction predicts a greater stabilisation of the Schottky defect relative to the O Frenkel. We infer from this that at the high defect concentrations associated with small supercell models the interactions between defects may have a stabilising effect.

To account for thermal effects, we also calculated defect-formation free energies ΔA_F from 0 K up to the melting temperature of ThO₂ (3630 K).⁶⁰

The Helmholtz free energies of formation, ΔA_F, of the Schottky and Frenkel defects are calculated as:

$$\Delta A_{f,\text{Schottky}} = A_{\text{Stoich}} - (A_{\text{Schottky}} + A_{\text{ThO}_2}) \quad (4)$$

$$\Delta A_{f,\text{Frenkel}} = A_{\text{Stoich}} - A_{\text{Frenkel}} \quad (5)$$

where A_{Stoich} , A_{Schottky} and A_{Frenkel} are the free energies of the supercell models of stoichiometric and defective ThO_2 , and A_{ThO_2} is the free energy of a single ThO_2 formula unit. All free energies are temperature dependent.

The Helmholtz energies in eqn (4)/(5) are calculated based on the phonon contributions to the free energy $A_{\text{vib}}(T)$, computed as:

$$\begin{aligned} A_{\text{vib}}(T) &= U_{\text{vib}}(T) - TS_{\text{vib}}(T) \\ &= -\frac{1}{N}k_{\text{B}}T \ln Z_{\text{vib}}(T) \\ &= \frac{1}{N} \left\{ \frac{1}{2} \sum_{qj} \hbar\omega_{qj} + k_{\text{B}}T \sum_{qj} \ln [1 - \exp(-\hbar\omega_{qj}/k_{\text{B}}T)] \right\} \end{aligned} \quad (6)$$

Here $Z_{\text{vib}}(T)$ is the vibrational partition function at temperature T , k_{B} is the Boltzmann constant, the sums run over phonon modes with frequency ω_{qj} indexed by a wavevector \mathbf{q} and a band index j , and the normalisation factor N is the number of unit cells in the crystal (equivalent to the number of \mathbf{q} in the summation). The internal energy and entropy of the phonon system, $U_{\text{vib}}(T)$ and $S_{\text{vib}}(T)$, are given by:

$$U_{\text{vib}}(T) = \sum_{qj} \hbar\omega_{qj} \left[\frac{1}{2} + \frac{1}{\exp(\hbar\omega_{qj}/k_{\text{B}}T) - 1} \right] \quad (7)$$

$$\begin{aligned} S_{\text{vib}}(T) &= \frac{1}{2T} \sum_{qj} \hbar\omega_{qj} \coth(-\hbar\omega_{qj}/2k_{\text{B}}T) - k_{\text{B}} \sum_{qj} \ln [2 \sinh(-\hbar\omega_{qj}/2k_{\text{B}}T)] \end{aligned} \quad (8)$$

The total Helmholtz energy of the system, $A(T)$, can then be computed by adding the lattice internal energy U_0 , which we equate to the DFT total energy:

$$A(T) = U_0 + A_{\text{vib}}(T) = U_0 + U_{\text{vib}}(T) - TS_{\text{vib}}(T) \quad (9)$$

Under the assumption of zero pressure, the Gibbs free energy $G(T)$ and the Helmholtz energy $A(T)$ can be equated.

However, as our calculation are performed at constant volume there may be a residual cell pressure in the defect models, and so we strictly work with $A(T)$. To determine the $A_{\text{vib}}(T)$ we use one of two methods. In method 1, we consider frequencies ω_{qj} sampled at wavevectors \mathbf{q} across the Brillouin zone. In Method 2, we consider only the ω_j at the zone centre $\mathbf{q} = \Gamma$. While an approximation, this simplified model is widely used for treating large unit cells where further supercell expansions to calculate frequencies at $\mathbf{q} \neq \Gamma$ without interpolation are not practical.

Fig. 2 shows the defect-formation free energies of the $\text{S}\langle 100 \rangle$, $\text{S}\langle 110 \rangle$, $\text{S}\langle 111 \rangle$, $\text{ThF}\langle 111 \rangle$ and $\text{OF}\langle 133 \rangle$ defects as a function of temperature calculated using method 1. The formation energies decrease with temperature, which implies that it is easier to

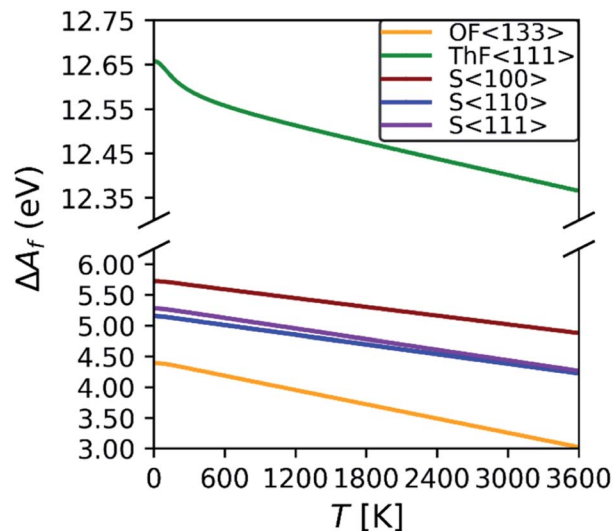


Fig. 2 Defect-formation free energies for the OF(133), ThF(111), S(100), S(110) and S(111) defects as a function of temperature calculated using method 1.

generate defects at elevated T . This is in line with experimental observations,⁵² which show that the generation of O Frenkel defects at higher temperatures leads to enhanced oxygen diffusion.²¹ Comparing the formation energies at $T = 0$ and 3630 K predicts decreases of 0.85–1.02 eV for the Schottky defects, 1.33 eV for the OF(133) defect, and 0.30 eV for ThF(111) defect. We therefore conclude that temperature effects are significant, but do not affect the overall stability trend. Method 2, using three different models for the contributions from the acoustic modes, predicts a small ~ 0.25 – 0.5 eV difference in the formation energies at $T = 3630$ K (see ESI†). For both methods the trend in stability ordering remains the same, with the defect formation energies in the order of $\text{OF} < \text{S} < \text{ThF}$.

To understand how the changes in the defect formation energies impact the defect concentrations N_{D} , we estimated the concentrations using the Boltzmann distribution:

$$N_{\text{D}} = N \times \exp(-\Delta A_f/k_{\text{B}}T) \quad (10)$$

where N is density of “sites”. Our defect formation energies are relative to the supercell, so $N = 1/V_{\text{SC}} = 7.10 \times 10^{20} \text{ cm}^{-3}$. We note that we do not account for degeneracies due to the equivalent O/Th sites in the supercell, which a crude estimate suggests could potentially increase the concentrations by between 10–100×. The temperature dependence of the concentrations of the three Schottky and the OF(133) and ThF(111) defects are shown in Fig. 3. Taking a concentration of $N_{\text{D}} = 1 \text{ cm}^{-3}$ as a threshold, we predict significant concentrations of OF to form at a much lower $T = 1030$ K than the more energetically unstable ThF defect ($T = 3000$ K).

C. Phonon dispersion and phonon density of states

Since the majority of the thermal transport in ThO_2 is through the phonons, an accurate description of the structural dynamics is crucial. The calculated phonon dispersion and atom-



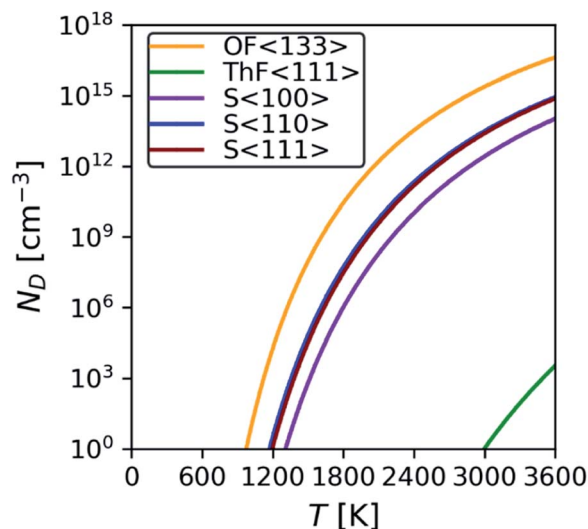


Fig. 3 Predicted defect concentrations as a function of temperature for the S(100), S(110), S(111), ThF(111) and OF(133) defects using the calculated defect formation free energies.

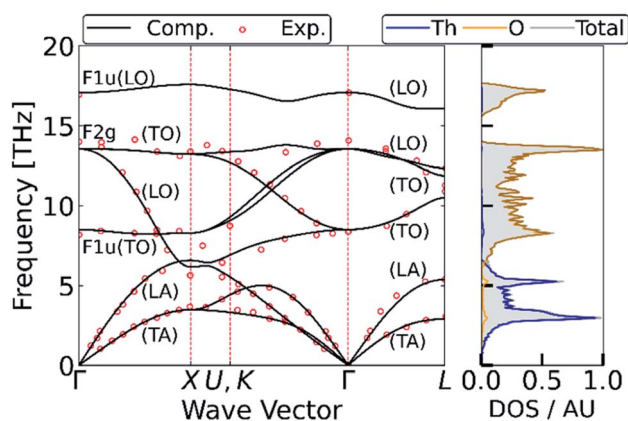


Fig. 4 Calculated phonon dispersion and atom-projected density of states of stoichiometric ThO₂. Inelastic neutron-scattering (INS) measurements from ref. 21 are overlaid as red dots.

projected density of states are shown in Fig. 4 and compared to data from inelastic neutron-scattering (INS) measurements.²¹ The ThO₂ primitive cell contains three atoms and the dispersion thus has three acoustic and six optic branches at each wavevector \mathbf{q} . The three lower-frequency acoustic modes split into longitudinal (LA) and transverse (TA) modes and are mainly attributed to motions of the heavier Th sublattice. The six higher-frequency optic modes again divide into longitudinal and transverse (LO/TO) modes and are predominantly associated with motion of the lighter O sublattice. The general features of the spectrum are common to UO₂ and PuO₂ and have been demonstrated in calculations using DFT⁶¹ and potential models,⁶² and in experimental time-of-flight INS measurements.^{61,63}

A list of modes and frequencies at each of the high-symmetry \mathbf{q} in the $Fm\bar{3}m$ Brillouin zone point is provided in Table 2 and compared to INS,^{21,64} Raman^{9,64–67} and IR^{68,69} measurements. At the

Γ point, stoichiometric ThO₂ has a doubly-degenerate TO mode at 8.5 THz (alternate motion of Th and O atoms), a triply-degenerate Raman-active mode at 13.6 THz (alternate motion of O), and a singly-degenerate LO mode at 17.1 THz (alternate motion of Th and O). These assignments are supported by previous work.⁷⁰ The predicted frequencies are also in excellent agreement with INS measurements collected at 273 K, with an average 6% and maximum 13% difference. The discrepancies may in part be attributed to the neglect of temperature effects (*i.e.* thermal expansion and higher-order anharmonicity) in our calculations.²⁴

The overlap between the LA and TO branches around $\mathbf{q} = X$ between ~ 6.2 – 6.6 THz was predicted for ThO₂ previously using LDA calculations,²³ and has also been predicted to occur in UO₂ and PuO₂ using LDA with dynamical mean-field theory (DMFT).¹² This feature is noteworthy because the acoustic modes tend to be the majority heat carriers, and the overlap with low-lying optic modes may facilitate enhanced phonon scattering and a reduced thermal conductivity in these materials.²³ For UO₂, the Debye approximation suggests that the F_{2g}(LO) mode only contributes 0.11 W m⁻¹ K⁻¹ along the LO branch from Γ to X, compared to 1.68 W m⁻¹ K⁻¹ along the LA branch.¹² Park *et al.* also found that the balance of the thermal transport shifts towards higher-frequency modes with shorter wavelengths at elevated temperature, resulting in reduced thermal transport.⁷³

While the phonon spectrum of stoichiometric ThO₂ is well documented in the literature,^{20–24,70} this is the first study to explore the impact of defects. The phonon dispersions of the defective structures, obtained in terms of the ThO₂ primitive cell using band unfolding,^{35,36} are shown together with the calculated PDOS in Fig. 5. In Table 3, we present estimates of the range of frequencies spanned by modes at the high-symmetry \mathbf{q} for comparison with Table 2.

The defective structures all show some degree of broadening across the phonon dispersion, including notable changes to the acoustic modes that are most pronounced along Γ –X direction around 2 THz. For the Frenkel defects (Fig. 5 D and E) the dispersions show notable mode softening at X around 6.6 THz. This suggests that the defects affect the vibrations of the O sublattice and have similar effects to the temperature-induced softening that occurs to this mode.²⁴ Ghosh *et al.*⁷¹ have linked reductions in the frequencies of the X-point phonon modes at 3.5 and 6.2 THz in ThO₂ to an increase in lattice strain, and have suggested that large strains lead to the phonon mode at 6.2 THz becoming imaginary. This effect has also been observed in CeO₂,⁷⁴ where the appearance of an imaginary mode under thermal expansion at high temperature predicates a superionic transition to a disordered oxygen sublattice. Taken together with our results, this provides a potential mechanism for how O Frenkel defects could enhance oxygen diffusion. We note however that while a mode softening is visible in Fig. 5E we do not observe an imaginary mode, which may be because we do not take into account temperature effects.

A handful of recent studies have investigated the effect of point defects on the phonon scattering in ThO₂, UO₂ and PuO₂.^{17,18,75} For ThO₂, non-equilibrium molecular dynamics simulations⁷⁵ found that Th and O vacancies affected the lower-frequency modes with the largest contributions to the thermal



Table 2 Calculated phonon frequencies (THz) of the modes at Γ , X and L in ThO₂ compared to data from other computational studies and experimental inelastic neutron-scattering (INS), Raman and IR measurements. Since predicted frequencies are often sensitive to the cell volume,⁷² we also show the predicted lattice constants from the computational studies

α_0 [Å]	Computational							Experimental			
	5.5605	5.618	5.619	5.60	5.30	5.5862	5.6202	INS ²¹	INS ⁶⁴	Raman ^{9,64–67}	IR ^{68,69}
Mode	PBEsol (this study)	PBE ⁷¹	PBE ²²	LDA + U ²⁰	LDA ²⁰	HSE06 (ref. 71)	SCAN ¹⁶	INS ²¹	INS ⁶⁴	Raman ^{9,64–67}	IR ^{68,69}
Γ : F _{1u} (LO)	17.1	16.6	16.6	16.3	16.5	16.8	17.4	16.9	17.2		16.7–17.2
Γ : F _{2g}	13.6	13.1	13.1	14.2	13.8	12.1	13.7	14.1	13.9	13.9–14.0	
Γ : F _{1u} (TO)	8.5	7.9	7.8	9.0	8.9	8.2	8.7	8.3	8.4		8.3–8.5
X	17.6	17.9	17.2	17.7	17.8	18.2	17.8	—	17.4		
	13.2	12.2	12.8	13.6	13.4	13.4	13.5	13.3	12.9		
	8.3	6.7	7.5	9.4	8.6	8.1	8.4	—	8.6		
	6.6	6.7	6.4	9.3	6.7	6.7	6.6	5.7	6.0		
	6.2	5.6	5.2	6.6	6.6	5.5	6.2	—	5.8		
	3.5	3.1	3.2	3.6	3.6	3.4	3.6	3.6	3.4		
L	16.1	16.2	15.5	16.4	16.4	16.5	16.3	—	17.4		
	12.4	11.8	11.9	12.8	12.8	12.6	12.7	12.2	11.7		
	11.9	11.5	11.3	12.7	12.1	12.0	12.1	11.2	11.3		
	10.5	9.7	9.9	11.0	10.7	10.5	10.8	10.7	9.8		
	5.4	5.2	5.0	5.6	5.7	5.3	5.5	5.3	5.3		
	2.9	2.6	2.7	2.9	3.0	2.9	2.9	2.9	3.0		

transport. Th vacancies were predicted to have a larger impact, with 0.1% Th and O vacancies predicted to induce 62 and 20% reductions in the thermal conductivity respectively. Comparing the PDOS curves of the defective models in Fig. 5 with the PDOS curve of pristine ThO₂ reveals an enhanced contribution from O at lower frequencies, suggesting that the defects may facilitate enhanced coupling between the O and Th sublattices. There are also some subtle changes to the DOS of the acoustic modes below ~ 2.5 THz, which may indicate changes in the number of phonon scattering pathways.

D. Infrared spectra

The Γ -point optic modes can be investigated using infrared (IR) and Raman spectroscopy. For stoichiometric ThO₂ there is a triply-degenerate Raman-active F_{2g} mode at 13.6 THz, a doubly-degenerate IR-active F_{1u} TO mode at 8.5 THz, and a singly-degenerate IR-active F_{1u} LO mode at 17.1 THz. Fig. 6 compares simulated IR spectra of pristine ThO₂ to the predicted spectra of the defective models. To allow for comparison between the spectra, and for compatibility with existing literature, we applied the nominal linewidth of 0.75 THz (including instrumental broadening) estimated from room-temperature IR reflectivity measurements.⁶⁹ We note however that our calculated intrinsic linewidths at $T = 300$ K are considerably sharper, at 0.034 and 0.098 THz for the F_{1u} and F_{2g} modes respectively. We attribute this in part to the difficulties inherent in extracting accurate linewidths from experimental spectra. However, we also note that the linewidths we calculate are the intrinsic linewidths due to three-phonon scattering. This approximation neglects higher-order scattering and additional linewidth contributions from phenomena such as phonon-defect scattering that may be present in experimental samples. We also

consider the structure at 0 K, and thermal expansion at finite temperature would usually narrow the phonon density of states and enhance the phonon scattering and linewidths.

The calculated frequencies of the F_{1u} TO and LO modes at 8.5 and 17.1 THz compare well to single-crystal measurements performed by Knight *et al.*⁶⁸ (8.4/17.6 THz) and Axe and Petit⁶⁹ (8.3/17.0 THz).

The defects break the symmetry of stoichiometric ThO₂ and result in some of the zone-boundary modes being “folded” to the Γ -point. This in turn leads to additional IR- and Raman-active modes in the defective systems, which are often associated with localised vibrations of atoms around the defect sites. As can be seen in Fig. 6B–F this results in more featured IR spectra. Inspection of the eigenvectors of the IR-active modes indicates that the vibrations are somewhat complex with contributions from both the Th and O sublattices.

Due to the much higher computational cost of calculating Raman activities, we were unable to predict Raman spectra for the defective models, but for completeness we show a simulated Raman spectrum of stoichiometric ThO₂ in Fig. S2.† The spectrum features a single peak at 13.6 THz from the F_{2g} mode, in line with other computational studies,^{16,20,22,71} but underestimated compared to the experimental literature.^{9,64–67}

E. Thermal conductivity

Using the single-mode relaxation time approximation (RTA) model, the macroscopic thermal conductivity $\kappa_{\text{latt}}(T)$ is obtained as a sum of contributions from individual phonon modes λ according to:⁴⁰

$$\kappa_{\text{latt}}(T) = \frac{1}{NV} \sum_{\lambda} \kappa_{\lambda}(T) = \frac{1}{NV} \sum_{\lambda} C_{\lambda}(T) v_{\lambda} \otimes v_{\lambda} \tau_{\lambda}(T) \quad (11)$$



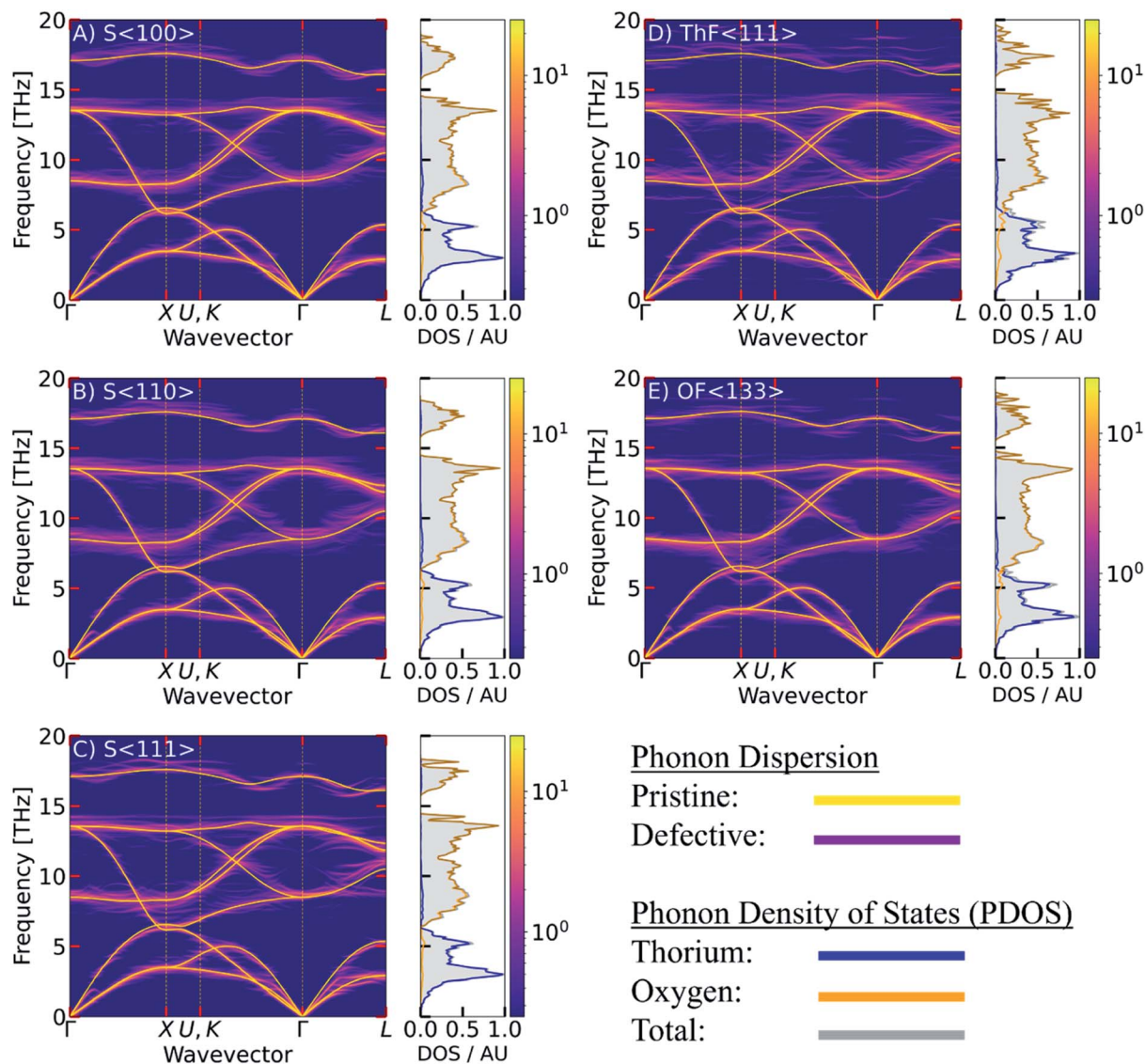


Fig. 5 Phonon dispersion curves and atom-projected density of states for the S(100), S(110) and S(111) (A–C), ThF(111) (D) and OF(133) (E) defect models. The spectral functions in the dispersion curves are shown on a logarithmic scale with the phonon dispersion of pristine ThO₂ overlaid as a yellow line. Each PDOS shows the total DOS in grey with the contributions from Th and O overlaid as blue and orange lines.

where C_λ are the modal heat capacities, v_λ are the group velocities, τ_λ are the lifetimes, V is the volume of the unit cell, and N is the number of wavevectors \mathbf{q} included in the summation. The C_λ are given by:

$$C_\lambda(T) = k_B \left(\frac{\hbar\omega_\lambda}{k_B T} \right) \frac{\exp[-\hbar\omega_\lambda/k_B T]}{(\exp[-\hbar\omega_\lambda/k_B T] - 1)^2} \quad (12)$$

where ω_λ are the phonon frequencies. The v_λ are given by:

$$v_\lambda = \frac{\delta\omega_\lambda}{\delta\mathbf{q}} = \frac{1}{2\omega_\lambda} \mathbf{W}_\lambda \left| \frac{\delta\mathbf{D}(\mathbf{q})}{\delta\mathbf{q}} \right| \mathbf{W}_\lambda \quad (13)$$

where the \mathbf{W}_λ are the phonon eigenvectors and $\mathbf{D}(\mathbf{q})$ is the dynamical matrix. Finally, the τ_λ are obtained from the phonon linewidths Γ_λ as:

$$\tau_\lambda(T) = \frac{1}{2\Gamma_\lambda(T)} \quad (14)$$

The Γ_λ are obtained as the imaginary part of the phonon self-energy using third-order perturbation theory, and the method is documented in detail in ref. 40. Computing the linewidths requires the third-order force constants, and obtaining these represents a substantial computational workload.

Since the κ_{latt} are tensor quantities, we discuss the scalar average of the diagonal elements, which we denote κ_{latt} in the following, *i.e.*

$$\kappa_{\text{latt}} = \frac{1}{3} \text{Tr}[\kappa_{\text{latt}}] = \frac{1}{3} [\kappa_{xx} + \kappa_{yy} + \kappa_{zz}] \quad (15)$$

We have omitted the explicit temperature dependence for brevity. The κ_{latt} are representative of what would be measured for a pressed pellet or polycrystal.

The thermal conductivity of ThO₂ is well studied in the literature using DFT^{23,24,70} and other theoretical



Table 3 Predicted frequency ranges (THz) of the Γ , X and L modes in the defective ThO₂ models considered in this work, estimated from the unfolded dispersions in Fig. 5, for comparison with the data for stoichiometric ThO₂ in Table 2

Mode	S<100>	S<110>	S<111>	OF<133>	ThF<111>
Γ	16.32–17.3	16.28–17.37	16.32–17.17	17.04–17.20	16.48–18.55
	13.39–14.32	13.15–14.35	13.32–14.23	13.00–14.45	13.1–14.65
	7.72–9.25	6.90–9.31	7.04–8.94	7.70–8.86	7.27–7.31, 8.17–9.84
X	17.2–18.63	17.43–18.22	17.39–18.09	17.24–18.48	17.27–19.59
	12.58–14.32	12.33–14.35	13.19–14.28	13.09–14.49	12.77–14.65
	7.56–9.26	6.90–9.09	6.90–9.46	6.98–9.16	7.06–10.01
	6.31–6.40	6.43–6.65	6.43–6.48	6.33–6.46	6.50–6.65
	6.04–6.15	6.19–6.29	6.17–6.24	5.24–5.51, 6.15–6.26	5.19–5.62, 6.19–6.41
	3.09–4.29	3.08–4.25	3.11–4.23	3.12–3.49	3.24–4.46
L	16.19–16.49	16.28–17.42	16.23–16.95	16.06–17.08	16.56–16.80
	12.13–13.41	12.09–13.46	12.32–13.37	12.20–14.45	12.19–14.48
	11.56–12.01	11.14–11.97	11.56–12.07	11.41–12.06	11.28–12.05
	8.27–9.42, 10.13–10.94	8.1–9.31, 10.04–10.97	8.13–8.94, 10.16–11.39	9.68–11.14	9.86–11.13
	4.98–5.37	5.04–5.38	4.74–5.24	5.13–5.42	5.27–5.62
	2.28–3.12	2.29–3.13	2.23–3.11	2.40–2.97	2.33–3.26

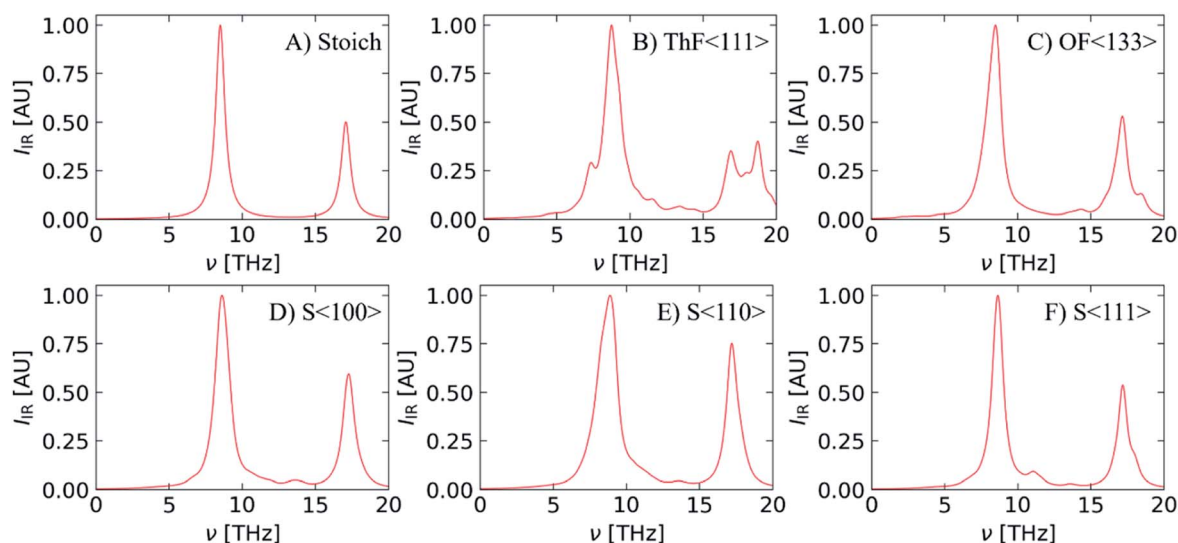


Fig. 6 Simulated IR spectra of stoichiometric ThO₂ (A) and models with Th (B) and O (C) Frenkel defects and one of three Schottky defect configurations (D–F). Each spectrum is generated with the nominal linewidth of 0.75 THz derived by Axe *et al.*⁶⁹

methods,^{22,42,70,76–79} and also in experiments.^{22,70,80–85} Fig. 7 compares the thermal conductivity of ThO₂ obtained using eqn (11) to a selection of experimental and theoretical works.

We predict a room-temperature (300 K) κ_{latt} of 20.8 W m⁻¹ K⁻¹, which compares reasonably well to the experimental measurements in ref. 70 (16.9 W m⁻¹ K⁻¹), ref. 80 (16.0 W m⁻¹ K⁻¹), and ref. 83 (15.7 W m⁻¹ K⁻¹). Given the scatter in the experiments, we suspect our prediction overestimates the measurements because it is difficult to prepare high-quality bulk samples that are free from defects such as grain boundaries – these defects limit the transport through modes with long mean free paths and thus reduce the overall κ_{latt} . In keeping with this, Mann *et al.*⁸⁶ obtained a room-temperature κ_{latt} between 18–20 W m⁻¹ K⁻¹ for single crystal ThO₂, which is higher than previous experimental results and closer to our prediction.

Our results are also consistent with other studies using DFT^{23,24} and potential models.^{42,70} At 300 K, the values of 20.6 and 17.9 W m⁻¹ K⁻¹ calculated using lattice dynamics coupled with the Boltzmann transport equation (LD-BTE)⁴² and equilibrium molecular dynamics (EMD)⁷⁰ respectively compare well with our value of 20.8 W m⁻¹ K⁻¹. The DFT study in ref. 23 used a similar technical setup to the present work and reported a value of 9.3 W m⁻¹ K⁻¹ at 600 K, which compares well to our prediction of 10 W m⁻¹ K⁻¹. However, we note that the choice of functional appears to have a significant impact, as the calculations in ref. 24 using the WC functional predicted a somewhat lower 7.7 W m⁻¹ K⁻¹.

To investigate the effect of crystal grain size on the thermal conductivity we employed a simple boundary-scattering model to limit the phonon mean free paths. As shown in Fig. 8, we find that beyond a grain size of 5 μm the thermal conductivity



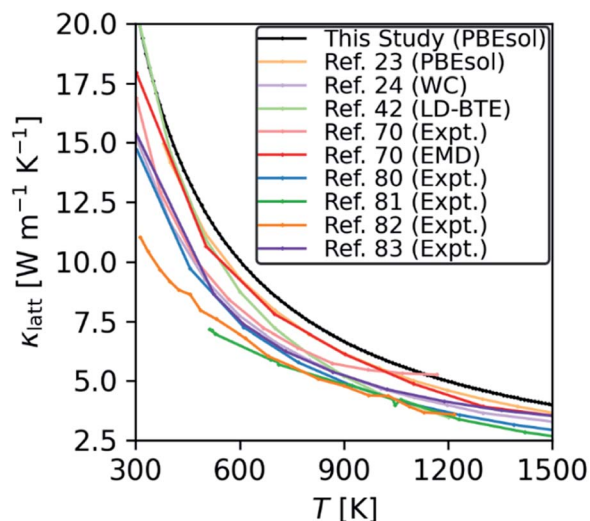


Fig. 7 Comparison of the κ_{latt} calculated for stoichiometric ThO_2 using the RTA model in eqn (11) with selected experimental and theoretical studies from the literature.

plateaus, in agreement with the findings of Nakamura and Machida.²³ At elevated temperature, the phonon mean free paths decrease and grain-boundary effects become less prominent. Although most experimental studies do not report a grain size, those that do indicate grain sizes in the range of 1–6 μm ,^{5,8,75} in which case we would not expect the grain size to have a significant impact on the κ_{latt} .

Computing the third-order force constants to calculate the phonon lifetimes of the defective structures would be prohibitively expensive and is therefore not feasible, so we explored instead the approximate models developed in ref. 41. We first consider the constant relaxation-time approximation (CRTA) model,^{41,87} where the τ_λ are replaced with a constant relaxation time, τ^{CRTA} according to:

$$\kappa_{\text{latt}} \approx \tau^{\text{CRTA}} \times \frac{1}{NV} \sum_{\lambda} \frac{\kappa_{\lambda}}{\tau_{\lambda}} = \tau^{\text{CRTA}} \times \frac{1}{NV} \sum_{\lambda} C_{\lambda} v_{\lambda} \otimes v_{\lambda} \quad (16)$$

We omit the temperature dependence of the terms for brevity but note that both the τ^{CRTA} and the summand are temperature dependent, the latter by virtue of the C_{λ} term (*c.f.* eqn (11)/(12)).

Since the terms in the summand are calculable from the harmonic force constants, this model allows for quantitative assessment of the impact of the defects on the κ_{latt} due to changes in the harmonic phonon frequencies and group velocities. Remarkably, we find that the defects reduce the harmonic term in eqn (16) by between 83.2 and 90.4% compared to stoichiometric ThO_2 at 600 K (Fig. 9). The $S\langle 111 \rangle$ defect is predicted by this model to have the smallest impact, whereas the two Frenkel defects have the largest impact. Given that the κ_{λ} in eqn (11) are proportional to the square of the group velocities, and eqn (12) is a shallow function of temperature, we can attribute these changes to disruption of the bonding network reducing the group velocities.

We next consider the approximate model for the phonon linewidths Γ_{λ} outlined in ref. 40. In the perturbative treatment the Γ_{λ} are obtained as a sum of three-phonon scattering processes between phonon triplets consisting of a reference mode λ and two interacting modes λ' and λ'' :

$$\Gamma_{\lambda} = \frac{18\pi}{\hbar^2} \sum_{\lambda'\lambda''} |\Phi_{-\lambda\lambda'\lambda''}|^2 \times \{ (n_{\lambda'} + n_{\lambda''} + 1) \delta(\omega - \omega_{\lambda'} - \omega_{\lambda''}) + (n_{\lambda'} - n_{\lambda''}) [\delta(\omega + \omega_{\lambda'} - \omega_{\lambda''}) - \delta(\omega - \omega_{\lambda'} - \omega_{\lambda''})] \} \quad (17)$$

In this equation the $\Phi_{\lambda\lambda'\lambda''}$ are the three-phonon interaction strengths, the n_{λ} are the occupation numbers given by,

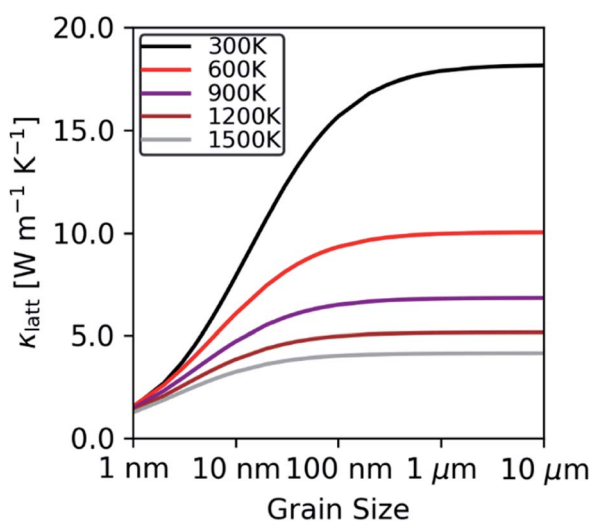


Fig. 8 Thermal conductivity of stoichiometric ThO_2 at $T = 300, 600, 900, 1200$ and 1500 K as a function of the crystal-grain size, predicted using a boundary-scattering model.

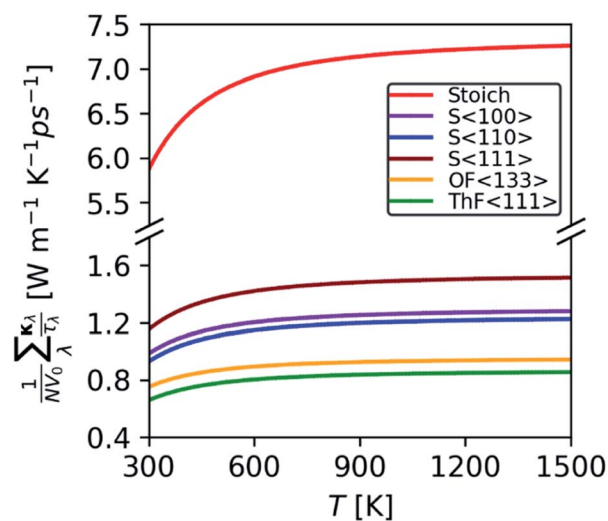


Fig. 9 Comparison of the harmonic function in eqn (16) calculated for the 96-atom stoichiometric ThO_2 supercell, three configurations of Schottky defects, and the lowest-energy O and Th Frenkel defects.



$$n_\lambda = \frac{1}{\exp[\hbar\omega_\lambda/k_B T] - 1} \quad (18)$$

$$P_\lambda = \frac{1}{(3n_a)^2} \sum_{\lambda'\lambda''} |\Phi_{-\lambda\lambda'\lambda''}|^2 \quad (20)$$

and the function δ enforces the conservation of energy. An approximate expression for the linewidths $\tilde{\Gamma}_\lambda$ can be written:⁴⁰

$$\tilde{\Gamma}_\lambda(\omega_\lambda) = \frac{18\pi}{\hbar^2} P_\lambda N_2(\mathbf{q}_\lambda, \omega_\lambda) \quad (19)$$

In this expression P_λ is the averaged phonon–phonon interaction strengths for the mode λ given by:

$$N_2(\mathbf{q}, \omega) = N_2^{(1)}(\mathbf{q}, \omega) + N_2^{(2)}(\mathbf{q}, \omega) \quad (21)$$

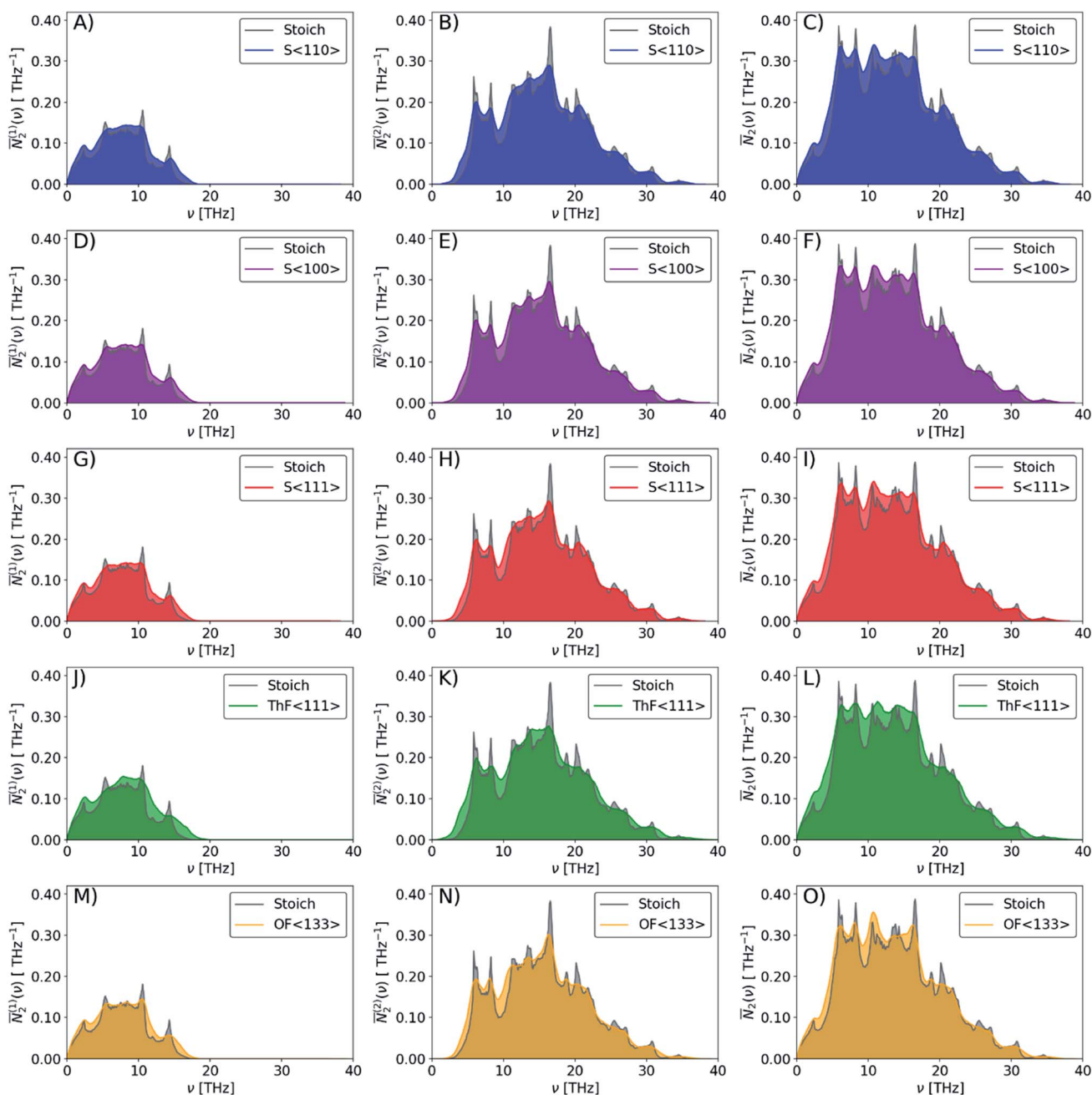


Fig. 10 Comparison of the weighted joint density of states (wJDOS) functions defined in eqn (21) for stoichiometric ThO₂ (grey) and the S(110) (blue), S(100) (purple), S(111) (red), ThF(111) (green) and OF(133) (orange) defect models. The first column (A/D/G/J/M) compares the $N_2^{(1)}$ for collision processes, the second column (B/E/H/K/N) compares the $N_2^{(2)}$ for decay processes, and the third column (C/F/I/L/O) compares the sum N_2 .



The two components $N_2^{(1)}(\mathbf{q}, \omega)$ and $N_2^{(2)}(\mathbf{q}, \omega)$ represent collision and decay (Class 1/Class 2) processes, respectively, and are defined as:

$$N_2^{(1)}(\mathbf{q}, \omega) = \frac{1}{N} \sum_{\lambda' \lambda''} \Delta(-\mathbf{q} + \mathbf{q}' + \mathbf{q}'') \times (n_{\lambda'} - n_{\lambda''}) [\delta(\omega + \omega_{\lambda'} - \omega_{\lambda''}) - \delta(\omega - \omega_{\lambda'} + \omega_{\lambda''})] \quad (22)$$

$$N_2^{(2)}(\mathbf{q}, \omega) = \frac{1}{N} \sum_{\lambda' \lambda''} \Delta(-\mathbf{q} + \mathbf{q}' + \mathbf{q}'') \times (n_{\lambda'} + n_{\lambda''} + 1) \delta(\omega - \omega_{\lambda'} - \omega_{\lambda''}) \quad (23)$$

where the function Δ enforces the conservation of (crystal) momentum.

This model serves two purposes. Firstly, the wJDOS functions can be calculated using the harmonic frequencies and enable a partial assessment of how changes in the phonon spectrum are likely to impact on the phonon linewidths and lifetimes. This is most easily done by averaging over \mathbf{q} to obtain a function of frequency only:

$$\bar{N}_2(\omega) = \bar{N}_2^{(1)}(\omega) + \bar{N}_2^{(2)}(\omega) = \frac{1}{N} \sum_{\mathbf{q}} N_2^{(1)}(\mathbf{q}, \omega) + \frac{1}{N} \sum_{\mathbf{q}} N_2^{(2)}(\mathbf{q}, \omega) \quad (24)$$

Secondly, if assume the P_λ in eqn (20) can be replaced with a constant value \tilde{P} , *e.g.* fitted for stoichiometric ThO₂, we can also predict an approximate κ_{latt} .⁴¹

The averaged wJDOS functions computed for ThO₂ and the defective systems are compared in Fig. 10. To allow for comparison between systems, we have normalized the functions by $(3n_a)^2$, which is folded into the P_λ term in eqn (19). Peaks in the $\bar{N}_2(\omega)$ at low frequencies are likely to indicate an enhanced broadening of the acoustic modes, which as noted above typically contribute the most to the thermal conductivity, leading to shorter lifetimes and suppressing the heat transport. Fig. 10 shows that the defects generally produce small increases in the $\bar{N}_2(\omega)$ at low frequencies, and thus suggests that changes to the phonon frequency spectrum may play a role in reducing the thermal conductivity.

To apply the approximate model in ref. 41 a value of $\tilde{P} = 9.722 \times 10^{13}$ was determined such that for the 96-atom stoichiometric supercell and a $10 \times 10 \times 10$ \mathbf{q} -point sampling the κ_{latt} for bulk ThO₂ at $T = 600$ K is recovered. Although the $\Phi_{\lambda\lambda'\lambda''}$ in eqn (17) are formally temperature independent, in practice the limitations of using a single value results in a weak temperature dependence, and so 600 K was chosen as a compromise. The κ_{latt} of pristine ThO₂ calculated using eqn (11), for the primitive cell, is compared to that obtained using the supercell model with the fitted \tilde{P} in Fig. S3.†

We note that the $10 \times 10 \times 10$ sampling mesh produces a harmonic function in eqn (16) that is $\sim 20\%$ smaller than for the primitive cell, indicating that the ν_λ are not fully converged with respect to the sampling mesh (Fig. S4†). We found that the

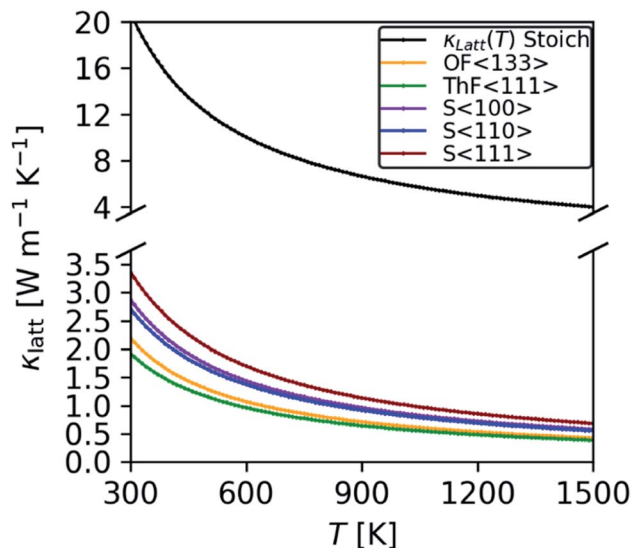


Fig. 11 Comparison of the κ_{latt} of the five defective models considered in this work calculated using the constant P_λ model with the \tilde{P} fitted for the stoichiometric ThO₂ supercell at $T = 600$ K.

harmonic function for the supercell was slow to converge with respect to the sampling mesh, and we were unable practically to increase it due to memory constraints. This is a technical limitation of the current implementation in Phonopy. However, we would expect a similar relative error for the defect supercells, and we also note that the fitted \tilde{P} may partially compensate for this issue.

Fig. 11 shows the thermal conductivity of the defective models predicted using this approximate model. Interestingly, we find the same 83.2–90.4% reductions in the κ_{latt} at 600 K as predicted by considering the harmonic function in eqn (16). This suggests that the small changes in the numbers of energy-conserving scattering channels suggested by the wJDOS functions in Fig. 10 do not have a material impact on the phonon lifetimes. While perhaps counter-intuitive, it is possible that the averaged functions in Fig. 10 will mask larger variation in the $N_2(\mathbf{q}, \omega)$ of individual wavevectors (*i.e.* increases and decreases in the modal κ_λ at different \mathbf{q} may compensate one another). As noted above, our relatively small defect supercells represent a significantly higher defect concentration than is likely to be achieved under thermal equilibrium (Fig. 3), and so the reduction in the κ_{latt} is unlikely to be as prominent in real materials. On the other hand, the significant energy release associated with nuclear decay events in working reactors is likely to produce regions with much larger non-equilibrium local concentrations of defects, and our predictions suggest these may form “hotspots” where heat cannot effectively be dissipated. This could have several important consequences, including cracking of the fuel rods as a result of accumulated thermal stresses and swelling due to accelerated release of fission gases.¹⁷

IV. Conclusions

In summary, we have performed a comprehensive study of the structure, energetics, lattice dynamics and thermal transport of



stoichiometric ThO₂ and models of the intrinsic Schottky and O/Th Frenkel defects.

First-principles DFT calculations predict that the O Frenkel defect is the most energetically favourable. We have identified a more stable configuration of the Th Frenkel defect, not found in previous studies, with the interstitial and vacancy arranged along the $\langle 111 \rangle$ rather than $\langle 201 \rangle$ direction. We have also investigated the phonon contributions to the thermodynamic free energy and found that these terms may selectively stabilise the defects relative to pristine ThO₂ and thereby reduce the defect formation energies at elevated temperature.

Our lattice-dynamics calculations demonstrate that the presence of defects leads to a significant broadening of the phonon dispersion and introduces additional IR-active modes that may serve as useful spectral signatures for identifying the defects in real materials using routine spectroscopy.

Finally, we also applied two approximate models to assess the impact of the defects on the thermal transport. We predict that the defects can reduce the (local) heat transport by as much as ~90% by disrupting the regular bonding network of the stoichiometric material and reducing the phonon group velocities. Interestingly, we also find that, within the approximation of a constant phonon-phonon interaction strength, the changes in the phonon spectra due to the presence of defects do not lead to significant changes to the phonon lifetimes. While verifying the predicted reduction in κ_{latt} would require explicit computation of the third-order force constants, it would be somewhat surprising if the defects led to so much weaker phonon-phonon interactions as to counteract the large reduction in the group velocities.

Overall, our modelling indicates that the presence of defects can have a significant impact on the thermal transport, and this is particularly significant in operating reactors where nuclear events are likely to lead to large non-equilibrium local defect concentrations. On the other hand, our results suggest that the impact on the thermal conductivity can be minimised if the defect concentrations can be controlled, which would improve the safety and performance profiles of the fuel. If the thermal performance of an alternative fuel material like ThO₂ could be made tolerant to the changes in its structure, *i.e.* to the formation of defects, then it is reasonable to suggest that this may be beneficial from a safety perspective compared to UO₂.⁸⁸ Further research in this direction will require reliable means to identify and quantify defects in real materials and to assess their impact on the physical properties; modelling can play an important role in this, for example, as we have shown, by identifying spectral signatures that could be measured using routine spectroscopic techniques.

Data availability

Raw data from these calculations may be obtained from the authors on reasonable request.

Author contributions

SM, JS, JST and MM performed the calculations and data analysis. JS and AT implemented and applied the band-

unfolding procedure. JF, DJC, ES and SCP provided support and discussion. RMH and MTS provided comment on the comparison with experiments. MM and JS devised the research project. All authors contributed to drafting and editing the manuscript.

Conflicts of interest

There are no conflicts of interest.

Acknowledgements

SM and MM acknowledge the University of Huddersfield (UoH) EPSRC-DTP competition 2018–19 (EP/R513234/1) for funding. JMS is grateful to UK Research and Innovation (UKRI) for the award of a Future Leaders Fellowship (MR/T043121/1), and to the University of Manchester (UoM) for the previous support of a UoM Presidential Fellowship. ELdS acknowledges financial support from the NECL project under NORTE-01-0145-FEDER-022096. Analysis was performed on the Orion computing facility at the UoH and on the Computational Shared Facility at UoM. Calculations were run on the ARCHER and ARCHER2 UK National Supercomputing Services *via* our membership of the UK HEC Materials Chemistry Consortium (MCC; EPSRC EP/L000202, EP/R029431). We would also like to acknowledge computing time granted through the EU PRACE DECI-16 16DECI0044 SDAAnOx project. To the extent that this paper relies on the contribution of RMH/MTS, then the copyright vests in the @British Crown Copyright 2020/AWE.

References

- 1 V. Masson-Delmotte, P. Zhai, A. Pirani, S. L. Connors, C. Péan, S. Berger, N. Caud, Y. Chen, L. Goldfarb, M. I. Gomis, M. Huang, K. Leitzell, E. Lonnoy, J. B. R. Matthews, T. K. Maycock, T. Waterfield, O. Yelekçi, R. Yu and B. Zhou, *Climate Change 2021: the Physical Science Basis, Contribution of Working Group I to the Sixth Assessment Report of the Intergovernmental Panel on Climate Change*, 2021.
- 2 J. S. Herring, P. E. MacDonald, K. D. Weaver and C. Kullberg, *Nucl. Eng. Des.*, 2001, **203**, 65–85.
- 3 M. Basu, R. Mishra, S. R. Bharadwaj and D. Das, *J. Nucl. Mater.*, 2010, **403**, 204–215.
- 4 R. K. Sinha and A. Kakodkar, *Nucl. Eng. Des.*, 2006, **236**, 683–700.
- 5 S. R. Spurgeon, M. Sassi, C. Ophus, J. E. Stubbs, E. S. Ilton and E. C. Buck, *Proc. Natl. Acad. Sci. U. S. A.*, 2019, **116**, 17181–17186.
- 6 M. Idiri, T. Le Bihan, S. Heathman and J. Rebizant, *Phys. Rev. B: Condens. Matter Mater. Phys.*, 2004, **70**, 014113.
- 7 L. G. Liu, *Earth Planet. Sci. Lett.*, 1980, **49**, 166–172.
- 8 J. P. Dancausse, E. Gering, S. Heathman and U. Benedict, *High Pressure Res.*, 1990, **2**, 381–389.
- 9 A. Jayaraman, G. A. Kourouklis and L. G. van Uitert, *Pramana*, 1988, **30**, 225–231.



- 10 B. T. M. Willis, *Proc. R. Soc. London, Ser. A*, 1963, **274**, 134–144.
- 11 B. A. Chidester, O. S. Pardo, R. A. Fischer, E. C. Thompson, D. L. Heinz, C. Prescher, V. B. Prakapenka and A. J. Campbell, *Am. Mineral.*, 2018, **103**, 749–756.
- 12 Q. Yin and S. Y. Savrasov, *Phys. Rev. Lett.*, 2008, **100**, 225504.
- 13 J. W. L. Pang, W. J. L. Buyers, A. Chernatynskiy, M. D. Lumsden, B. C. Larson and S. R. Phillpot, *Phys. Rev. Lett.*, 2013, **110**, 157401.
- 14 W. R. Deskins, A. Hamed, T. Kumagai, C. A. Dennett, J. Peng, M. Khafizov, D. Hurley and A. El-Azab, *J. Appl. Phys.*, 2021, **129**, 075102.
- 15 C. A. Dennett, Z. Hua, A. Khanolkar, T. Yao, P. K. Morgan, T. A. Prusnick, N. Poudel, A. French, K. Gofryk, L. He, L. Shao, M. Khafizov, D. B. Turner, J. M. Mann and D. H. Hurley, *APL Mater.*, 2020, **8**, 111103.
- 16 C. A. Dennett, W. R. Deskins, M. Khafizov, Z. Hua, A. Khanolkar, K. Bawane, L. Fu, J. M. Mann, C. A. Marianetti, L. He, D. H. Hurley and A. El-Azab, *Acta Mater.*, 2021, **213**, 116934.
- 17 K. Mitchell, J. Park, A. Resnick, H. Horner and E. B. Farfan, *Appl. Sci.*, 2020, **10**, 1860.
- 18 A. Resnick, K. Mitchell, J. Park, E. B. Farfan and T. Yee, *Nucl. Eng. Technol.*, 2019, **51**, 1398–1405.
- 19 M. Khafizov, M. F. Riyad, Y. Wang, J. Pakarinen, L. He, T. Yao, A. El-Azab and D. Hurley, *Acta Mater.*, 2020, **193**, 61–70.
- 20 C. Sevik and T. Çağın, *Phys. Rev. B: Condens. Matter Mater. Phys.*, 2009, **80**, 014108.
- 21 K. Clausen, W. Hayes, J. E. Macdonald, R. Osborn, P. G. Schnabel, M. T. Hutchings and A. Magerl, *J. Chem. Soc. Faraday Trans. 2*, 1987, **83**, 1109.
- 22 Y. Lu, Y. Yang and P. Zhang, *J. Phys. Condens. Matter*, 2012, **24**, 225801.
- 23 H. Nakamura and M. Machida, *J. Nucl. Mater.*, 2019, **519**, 45–51.
- 24 B. Szpunar and J. A. Szpunar, *Solid State Sci.*, 2014, **36**, 35–40.
- 25 G. Kresse and J. Furthmüller, *Phys. Rev. B: Condens. Matter Mater. Phys.*, 1996, **54**, 11169–11186.
- 26 J. Heyd, G. E. Scuseria and M. Ernzerhof, *J. Chem. Phys.*, 2003, **118**, 8207–8215.
- 27 J. Heyd, G. E. Scuseria and M. Ernzerhof, *J. Chem. Phys.*, 2006, **124**, 219906.
- 28 J. P. Perdew, A. Ruzsinszky, G. I. Csonka, O. A. Vydrov, G. E. Scuseria, L. A. Constantin, X. Zhou and K. Burke, *Phys. Rev. Lett.*, 2008, **100**, 136406.
- 29 A. E. Shields, D. Santos-Carballal and N. H. de Leeuw, *J. Nucl. Mater.*, 2016, **473**, 99–111.
- 30 B. T. Wang, P. Zhang, H. Song, H. Shi, D. Li and W. D. Li, *J. Nucl. Mater.*, 2010, **401**, 124–129.
- 31 Y. Lu, D. F. Li, B. T. Wang, R. W. Li and P. Zhang, *J. Nucl. Mater.*, 2011, **408**, 136–141.
- 32 X. D. Wen, R. L. Martin, L. E. Roy, G. E. Scuseria, S. P. Rudin, E. R. Batista, T. M. McCleskey, B. L. Scott, E. Bauer, J. J. Joyce and T. Durakiewicz, *J. Chem. Phys.*, 2012, **137**, 154707.
- 33 H. J. Monkhorst and J. D. Pack, *Phys. Rev. B: Solid State*, 1976, **13**, 5188.
- 34 A. Togo and I. Tanaka, *Scr. Mater.*, 2015, **108**, 1–5.
- 35 P. B. Allen, T. Berlijn, D. A. Casavant and J. M. Soler, *Phys. Rev. B: Condens. Matter Mater. Phys.*, 2013, **87**, 085322.
- 36 P. B. Allen, T. Berlijn, D. A. Casavant and J. M. Soler, *Phys. Rev. B: Condens. Matter Mater. Phys.*, 2013, **87**, 239904.
- 37 M. Gajdoš, K. Hummer, G. Kresse, J. Furthmüller and F. Bechstedt, *Phys. Rev. B: Condens. Matter Mater. Phys.*, 2006, **73**, 045112.
- 38 J. Skelton, *Phonopy-Spectroscopy*, <https://github.com/JMSkelton/Phonopy-Spectroscopy>, (accessed 11 June 2020).
- 39 J. M. Skelton, L. A. Burton, A. J. Jackson, F. Oba, S. C. Parker and A. Walsh, *Phys. Chem. Chem. Phys.*, 2017, **19**, 12452–12465.
- 40 A. Togo, L. Chaput and I. Tanaka, *Phys. Rev. B: Condens. Matter Mater. Phys.*, 2015, **91**, 094306.
- 41 J. M. Skelton, *J. Mater. Chem. C*, 2021, **9**, 11772–11787.
- 42 R. K. Behera and C. S. Deo, *J. Phys. Condens. Matter*, 2012, **24**, 215405.
- 43 S. T. Murphy, M. W. D. Cooper and R. W. Grimes, *Solid State Ionics*, 2014, **267**, 80–87.
- 44 M. W. D. Cooper, M. J. D. Rushton and R. W. Grimes, *J. Phys. Condens. Matter*, 2014, **26**, 105401.
- 45 K. Govers, S. Lemehov, M. Hou and M. Verwerft, *J. Nucl. Mater.*, 2007, **366**, 161–177.
- 46 V. K. Tripathi and R. Nagarajan, *Inorg. Chem.*, 2016, **55**, 12798–12806.
- 47 F. Hund and W. Dürrwächter, *J. Inorg. Gen. Chem.*, 1951, **265**, 67–72.
- 48 H. J. Whitfield, D. Roman and A. R. Palmer, *J. Inorg. Nucl. Chem.*, 1966, **28**, 2817–2825.
- 49 K. Clausen, W. Hayes, J. E. Macdonald, P. Schnabel, M. T. Hutchings and J. K. Kjems, *High. Temp. - High. Press.*, 1983, **15**, 383–390.
- 50 W. A. Lambertson, M. H. Mueller and F. H. Gunzel, *J. Am. Ceram. Soc.*, 1953, **36**, 397–399.
- 51 A. K. Tyagi and M. D. Mathews, *J. Nucl. Mater.*, 2000, **278**, 123–125.
- 52 G. E. Murch and C. R. A. Catlow, *J. Chem. Soc., Faraday Trans. 2*, 1987, **83**, 1157–1169.
- 53 R. J. M. Konings and O. Beneš, *J. Phys. Chem. Solids*, 2013, **74**, 653–655.
- 54 K. Ando, Y. Oishi and Y. Hidaka, *J. Chem. Phys.*, 2008, **65**, 2751.
- 55 M. Nadeem, M. Akhtar, R. Shaheen, M. Haque and A. Y. Khan, *J. Mater. Sci. Technol.*, 2001, **17**, 638.
- 56 M. Osaka, J. Adachi, K. Kurosaki, M. Uno and S. Yamanaka, *J. Nucl. Sci. Technol.*, 2007, **44**, 1543–1549.
- 57 P. Martin, D. J. Cooke and R. Cywinski, *J. Appl. Phys.*, 2012, **112**, 073507.
- 58 J. P. Crocombette, F. Jollet, L. T. Nga and T. Petit, *Phys. Rev. B: Condens. Matter Mater. Phys.*, 2001, **64**, 104107.
- 59 Y. Yun, P. M. Oppeneer, H. Kim and K. Park, *Acta Mater.*, 2009, **57**, 1655–1659.
- 60 E. Hashem, A. Seibert, J. F. Vigier, M. Naji, S. Mastromarino, A. Cicciooli and D. Manara, *J. Nucl. Mater.*, 2019, **521**, 99–108.



- 61 J. W. L. Pang, A. Chernatynskiy, B. C. Larson, W. J. L. Buyers, D. L. Abernathy, K. J. McClellan and S. R. Phillpot, *Phys. Rev. B: Condens. Matter Mater. Phys.*, 2014, **89**, 115132.
- 62 A. S. Poplavnoi, T. P. Fedorova and I. A. Fedorov, *Phys. Solid State*, 2017, **59**, 766–772.
- 63 G. Dolling, R. A. Cowley and A. D. B. Woods, *Can. J. Phys.*, 1965, **43**, 1397–1413.
- 64 M. S. Bryan, L. Fu, K. Rickert, D. Turner, T. A. Prusnick, J. M. Mann, D. L. Abernathy, C. A. Marianetti and M. E. Manley, *Commun. Phys.*, 2020, **3**, 1–7.
- 65 S. Kern and C. Y. She, *Chem. Phys. Lett.*, 1974, **25**, 287–289.
- 66 V. G. Keramidias and W. B. White, *J. Chem. Phys.*, 1973, **59**, 1561–1562.
- 67 K. Kamali, K. Ananthasivan, T. R. Ravindran and D. S. Kumar, *J. Nucl. Mater.*, 2017, **493**, 77–83.
- 68 S. Knight, R. Korlacki, C. Dugan, J. C. Petrosky, A. Mock, P. A. Dowben, J. Matthew Mann, M. M. Kimani and M. Schubert, *J. Appl. Phys.*, 2020, **127**, 125103.
- 69 J. D. Axe and G. D. Pettit, *Phys. Rev.*, 1966, **151**, 676–680.
- 70 L. Malakkal, A. Prasad, E. Jossou, J. Ranasinghe, B. Szpunar, L. Bichler and J. Szpunar, *J. Alloys Compd.*, 2019, **798**, 507–516.
- 71 P. S. Ghosh, A. Arya, G. K. Dey, N. Kuganathan and R. W. Grimes, *Phys. Chem. Chem. Phys.*, 2016, **18**, 31494–31504.
- 72 J. M. Skelton, D. Tiana, S. C. Parker, A. Togo, I. Tanaka and A. Walsh, *J. Chem. Phys.*, 2015, **143**, 064710.
- 73 J. Park, E. B. Farfán and C. Enriquez, *Nucl. Eng. Technol.*, 2018, **50**, 731–737.
- 74 J. Buckeridge, D. O. Scanlon, A. Walsh, C. R. A. Catlow and A. A. Sokol, *Phys. Rev. B: Condens. Matter Mater. Phys.*, 2013, **87**, 214304.
- 75 J. Park, E. B. Farfán, K. Mitchell, A. Resnick, C. Enriquez and T. Yee, *J. Nucl. Mater.*, 2018, **504**, 198–205.
- 76 H. Y. Xiao, Y. Zhang and W. J. Weber, *Acta Mater.*, 2013, **61**, 467–476.
- 77 M. W. D. Cooper, S. C. Middleburgh and R. W. Grimes, *J. Nucl. Mater.*, 2015, **466**, 29–35.
- 78 M. J. Rahman, B. Szpunar and J. A. Szpunar, *Mater. Res. Express*, 2017, **4**, 075512.
- 79 J. Liu, Z. Dai, X. Yang, Y. Zhao and S. Meng, *J. Nucl. Mater.*, 2018, **511**, 11–17.
- 80 K. Bakker, E. H. P. Cordfunke, R. J. M. Konings and R. P. C. Schram, *J. Nucl. Mater.*, 1997, **250**, 1–12.
- 81 C. Cozzo, D. Staicu, J. Somers, A. Fernandez and R. J. M. Konings, *J. Nucl. Mater.*, 2011, **416**, 135–141.
- 82 C. G. S. Pillai and P. Raj, *J. Nucl. Mater.*, 2000, **277**, 116–119.
- 83 M. Saoudi, D. Staicu, J. Mouris, A. Bergeron, H. Hamilton, M. Naji, D. Freis and M. Cologna, *J. Nucl. Mater.*, 2018, **500**, 381–388.
- 84 T. R. G. Kutty, R. V. Kulkarni, P. Sengupta, K. B. Khan, K. Bhanumurthy, A. K. Sengupta, J. P. Panakkal, A. Kumar and H. S. Kamath, *J. Nucl. Mater.*, 2008, **373**, 309–318.
- 85 M. Murabayashi, Y. Takahashi and T. Mukaibo, *J. Nucl. Sci. Technol.*, 1969, **6**, 657–662.
- 86 M. Mann, D. Thompson, K. Serivalsatit, T. M. Tritt, J. Ballato and J. Kolis, *Cryst. Growth Des.*, 2010, **10**, 2146–2151.
- 87 J. Tang and J. M. Skelton, *J. Phys. Condens. Matter*, 2020, **33**, 164002.
- 88 D. H. Hurley, A. El-Azab, M. S. Bryan, M. W. D. Cooper, C. A. Dennett, K. Gofryk, L. He, M. Khafizov, G. H. Lander, M. E. Manley, J. M. Mann, C. A. Marianetti, K. Rickert, F. A. Selim, M. R. Tonks and J. P. Wharry, *Chem. Rev.*, 2021, DOI: 10.1021/acs.chemrev.1c00262.

